Fibers and Polymers (2023) 24:3657–3671
https://doi.org/10.1007/s12221-023-00249-x

Online ISSN 1875-0052
Print ISSN 1229-9197

REGULAR ARTICLE

The Effect of Thermal Treatment on the Morphology and Structure of SnO_2/TiO_2 Composite Micro-fibers

David Sanchez[1] · Jason Parsons[2] · Mataz Alcoutlabi[1]

Received: 29 November 2022 / Revised: 5 April 2023 / Accepted: 24 April 2023 / Published online: 15 August 2023

Abstract

Tin oxide and titanium oxide (SnO_2/TiO_2) composite fibers were prepared from polyvinylpyrrolidone (PVP)/SnO_2/TiO_2 precursor solutions with different SnO_2 to TiO_2 ratios of 1:1, 2:1, 3:1, and 3:2. The precursor fibers were thermally treated using different heating rates to prepare SnO_2/TiO_2 fibers with micro-belt morphology. The characterization of the SnO_2/TiO_2 composite fibers was performed using a scanning electron microscope (SEM), energy dispersive X-ray spectroscopy (EDS), X-ray diffraction (XRD), X-ray photoelectron spectroscopy (XPS), Raman spectroscopy, and thermogravimetric analysis (TGA). The SEM images showed that the fibers were flat and had micron-sized diameters. EDS mapping of the precursor fibers showed the fibers to have a distribution of Sn and Ti throughout the surface with areas of high concentration of carbon, nitrogen, and oxygen. The XRD, XPS, and Raman data confirmed the presence of SnO_2/TiO_2. Initial electrochemical testing of Li-ion half cells, using SnO_2/TiO_2 as anode material, showed the composite fibers with different ratios to have higher specific capacity and slower anode pulverization than SnO_2. The results reported in this work showed that SnO_2/TiO_2 composite fibers with micro-belt morphology could be achieved, and the synthesis was susceptible to both the temperature ramp rate during calcination of the precursor fibers and the SnO_2 to TiO_2 ratio in the composite fibers.

Keywords SnO_2 · Lithium-ion battery · Centrifugal spinning · Micro-belts · TiO_2

1 Introduction

Nanofibers have been widely used for their flexibility, affordability, and ease of production for many applications, such as water purification, air filtration, sensors, and various biomedical applications [1]. The ease of production of these fibers has been mainly due to the methods used: drawing, template synthesis, self-assembly, and electrospinning [2]. Electrospinning has been a popular method recently, but the method of Centrifugal Spinning (CS) has been gaining attention recently due to its versatility in using different solutions and melts [3–7]. CS uses centrifugal forces to expel a polymer solution (or melt) through a spinneret causing long fibers to be collected on surrounding pillars. CS produces fibers similar to electrospinning but at a higher production rate making it a newly popular method [8, 9].

The fiber morphology and structure tremendously affect their properties and performance. For example, long nanofibers have been used in the biomedical field for their flexibility and size in applications such as wound dressings, tissue scaffolds, and even localized drug delivery [10]. Fibers from CS can also be prepared into thin mats forming membranes to be used as filtration systems for dye waste-water treatment, and as water softening for pharmaceutical applications [11]. Fibers have been calcined forming short flat fibers known as nanobelts that have different properties, which can be used in applications such as gas sensors [12–15], anode materials for lithium-ion batteries [16–20], photocatalysts [13, 21], antibacterial agent [22], and supercapacitors [23]. The wide-range success of micro-belts is attributed to their one-dimensional structure as well as their physical and electronic properties [12, 15].

Additionally, multiple materials have been studied to prepare metal oxide composite fibers from multi-phase precursor solutions that would pair well and complement each other. Wang et al. conducted experiments to evaluate

✉ Mataz Alcoutlabi
mataz.alcoutlabi@utrgv.edu

[1] Department of Mechanical Engineering, University of Texas, Rio Grande Valley, 1201 W University Dr., Edinburg, TX 78539, USA

[2] Department of Chemistry, University of Texas, Rio Grande Valley, 1 W University Blvd., Brownsville, TX 78521, USA

the gas-sensing properties of three different metal oxides (tin oxide, zinc oxide, and indium oxide) and compared the results to those reported on three different composite combinations (tin oxide/zinc oxide, tin oxide/indium oxide, and zinc oxide/indium oxide) [24]. The results showed that the tin oxide/zinc oxide and tin oxide/indium oxide composites had a greater sensitivity to ethanol vapor than their counterparts, while the zinc oxide/indium oxide composite had a lower sensitivity. The team attributed these results to how well the composites' catalytic actions react [24].

Recent results reported on the synthesis of SnO_2/TiO_2 micro-belts composite showed that SnO_2 was an excellent material for gas sensing and lithium storage but has poor conductivity [12, 15, 19]. TiO_2 has been a great addition to SnO_2 for its stability due to its robust structure support [19]. Van Duy et al. prepared a 3:7 mol ratio SnO_2/TiO_2 solution by the sol–gel method and was sonicated with carbon nanotubes to achieve uniform thin films. The results showed that the SnO_2/TiO_2 composite had excellent sensitivity at different operating temperatures. The excellent sensitivity was attributed to the SnO_2 reaction with the gas molecules at a temperature around 250 °C, while the TiO_2 reacted with the gas molecules at 380 °C [25].

The formation of micro-belts, specifically when using different percentages of SnO_2/TiO_2 precursors is very sensitive to the heat treatment used during synthesis. This work focuses on the effect of heat treatment and specifically on the effect of temperature ramp-up rates during calcination on both the morphology and formation of SnO_2/TiO_2 micro-belts using different SnO_2 to TiO_2 ratios. The SnO_2/TiO_2 composite fibers were prepared by the centrifugal spinning of SnO_2/TiO_2 precursor solutions containing PVP and subsequent heat treatment at 700 °C.

2 Experimental

2.1 Material

Polyvinylpyrrolidone (PVP) ($Mw \sim 1{,}300{,}000$), polyacrylonitrile (PAN) (Mw 150,000), N, N-dimethyl formamide (DMF), SuperP carbon black, titanium (IV) butoxide (reagent grade, 97%), and tin (II) 2-ethylhexanoate were purchased from Sigma-Aldrich. Absolute Ethanol (200 proof) was purchased from Fisher Scientific. All these chemicals were used as is without further purification.

2.2 Micro-belt Preparation

20 g solutions of ethanol and PVP with weight concentrations of 85% and 15%, respectively, were prepared to obtain long fibers. SnO_2 and TiO_2 precursors were mixed with 50 wt.% PVP to prepare solutions with four different SnO_2 to TiO_2 ratios: (1:1), (2:1), (3:1), and (3:2). The solutions were magnetically stirred for 24 h and then centrifugally spun using a spinneret equipped with 30-gauge needles. Rotational speeds of 9000 rpm were used at 2 min intervals until the 20 g solutions were spun completely. The fibrous mats were collected and dried at room temperature for 24 h. The mats were then placed in an oven to be calcined at 700 °C for 3 h. Different ramp-up rates between 0.5 to 3.3 °C/min were used during the calcination process of the SnO_2/TiO_2 fibers.

Additionally, the SnO_2/TiO_2 micro-belts with different ratios were mixed into a PAN/carbon black slurry with a ratio of 8:1:1 (active material, PAN, and carbon black, respectively), using DMF as a solvent, and prepared for use as anode material in lithium-ion batteries. The slurry mixture was applied as a thin film onto a copper foil to dry in vacuum for 24 h. The copper foil was then placed in a tube furnace (MTI Corporation, OTF-1200X) at a temperature of 450 °C for 5 h. The copper foil was then cut into 1/2" diameter anodes and assembled into a Li-ion half-cell. The electrochemical performance of the SnO_2/TiO_2 composite anodes was investigated using Li-ion half cells (2032 coin-type cells). Lithium metal-foil was used as the counter electrode, while glass microfibers (Whatman 934-AH) were used as the separator. The electrolyte was made from 1 M of LiFP6 in ethylene carbonate (EC): dimethyl carbonate (DMC) (1:1 v/v). The Li-ion half cells were assembled in a high-purity argon-filled glove box (Mbraun, USA) with O_2 and H_2O concentrations of < 0.5 ppm. The electrochemical performance was evaluated by carrying out galvanostatic charge–discharge experiments on the Li-half (coin) cells at a current density of 100 mAg^{-1} between 0.05 and 3.0 V using the LANHE CT2001A battery testing system.

2.3 Structure Characterization

The morphology and elemental composition of the SnO_2/TiO_2 micro-belts were studied by scanning electron microscope (SEM) using a Sigma VP Carl Zeiss instrument (Germany), equipped with an energy-dispersive X-ray spectrometer (EDS) from EDAX (Mahwah, NJ, USA) to analyze the elemental composition of the composite fibers. The samples were sputter coated with a thin layer of gold and palladium using Denton's Desk V deposition system. The crystal structure of the micro-belts was examined using X-ray diffraction spectroscopy (XRD) and Raman Spectroscopy. The Raman data were collected using a BWTEK MiniRam II, equipped with a 785 nm laser, and a power of 500 W. The spectrometer has a 10 cm^{-1} resolution. A Bruker D2 powder (Bruker Germany) X-ray diffractometer was used with a Co source (Kα 1.789 Å). The data were collected in 2θ from 10 to 70° with a count time of 5 s and a step of 0.05° in 2θ. X-ray photoelectron spectroscopy (XPS) analysis was performed to determine the elemental composition at the

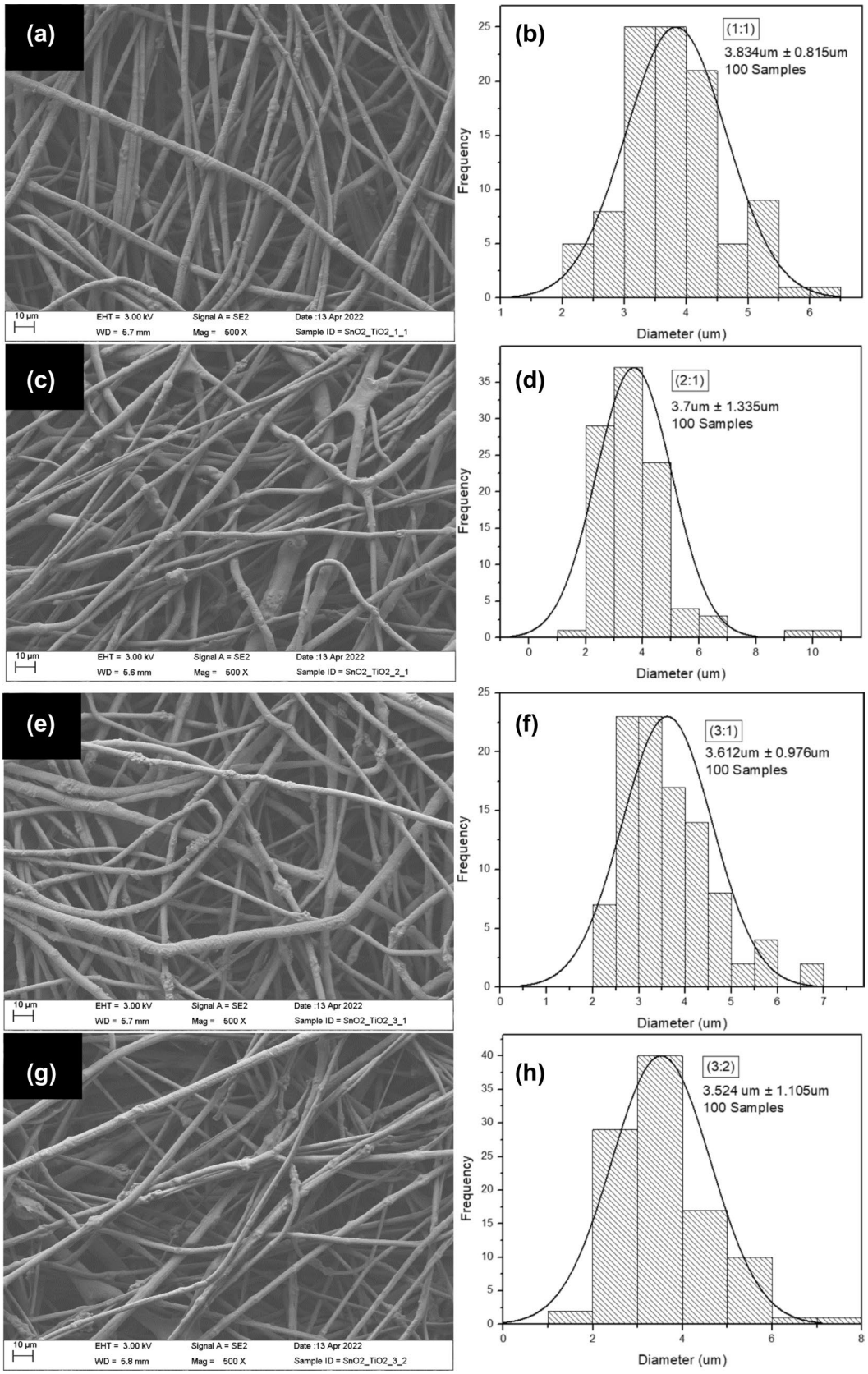

Fig. 1 SEM images and histograms of SnO_2/TiO_2/PVP fibers at different SnO_2 to TiO_2 ratios: **a** 1:1, **c** 2:1, **e** 3:1, **g** 3:2

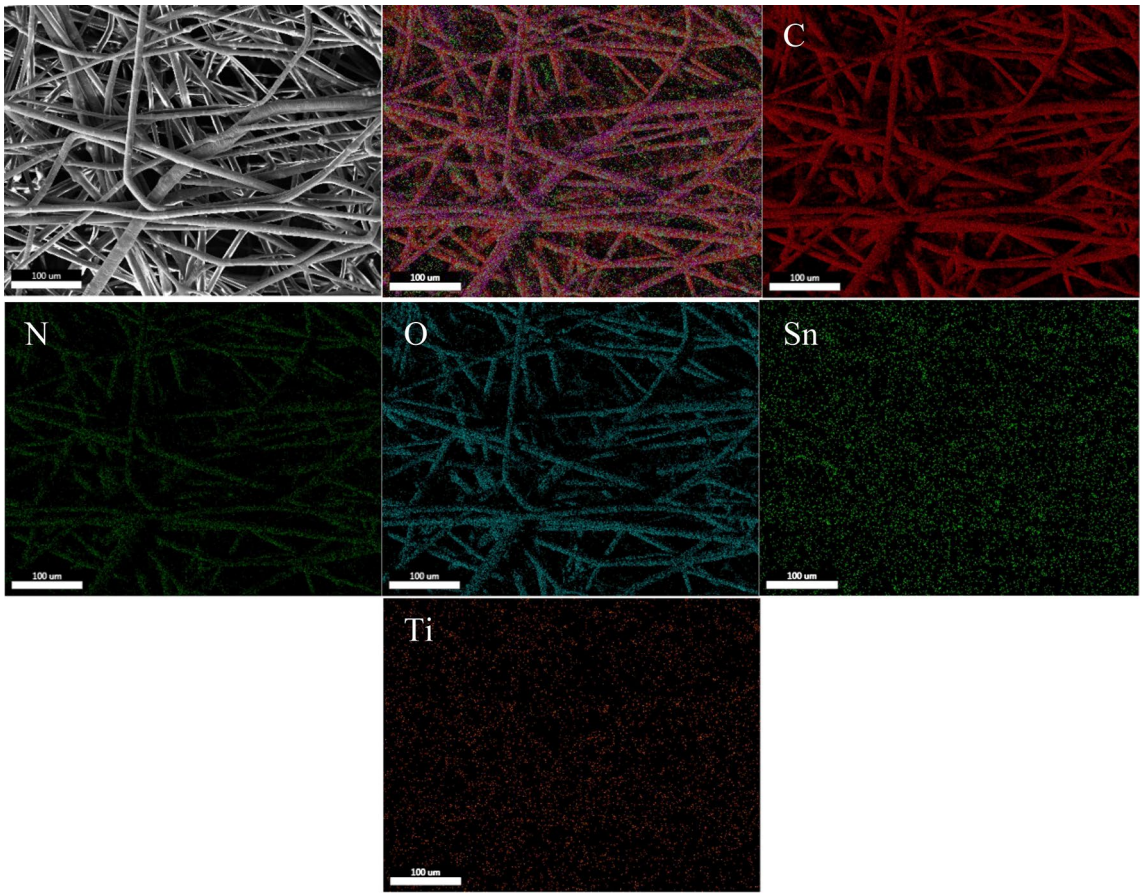

Fig. 2 EDS mappings of SnO_2/TiO_2/PVP fibers (1:1)

Table 1 EDS results of SnO_2/TiO_2 (1:1) pre-calcined fibers

Element	Weight %	Atomic %	Net Int	Error %	Kratio	*Z*	*A*	*F*
C K	59.82	86.74	607.92	5.49	0.5246	1.1714	0.7487	1.0000
O K	7.50	8.16	48.31	22.08	0.0279	1.1091	0.3355	1.0000
AuM	15.47	1.37	69.85	12.00	0.1044	0.5740	1.1707	1.0045
SnL	11.66	1.71	24.52	27.47	0.0771	0.6430	1.0269	1.0011
TiK	5.56	2.02	13.45	30.69	0.0449	0.8254	0.9836	0.9954

Table 2 EDS results of SnO_2/TiO_2 (3:2) calcined fibers

Element	Weight %	Atomic %	Net Int	Error %	Kratio	*Z*	*A*	*F*
C K	3.40	13.52	92.60	5.21	0.0358	1.4873	0.7068	1.0000
N K	2.28	7.75	48.20	5.94	0.0231	1.4483	0.7017	1.0000
O K	11.98	35.71	261.60	8.21	0.0663	1.4144	0.3916	1.0000
SnL	65.63	26.38	483.40	3.31	0.5750	0.8570	1.0198	1.0024
TiK	16.71	16.64	147.70	5.00	0.1691	1.0967	0.9196	1.0036

surface of the micro-belts. The XPS spectra were collected using Thermoscientific K-α instrument equipped with monochromatized Al Kα radiation (1486.7 eV). The thermal degradation of the SnO_2/TiO_2 precursor fibers was investigated by thermogravimetric analysis (TGA) (Netzch TG 209 F3 Tarsus) in air environment with temperatures from 25 to 700 °C at a heating rate of 5 °C/min. The pre-calcined fibers were sprayed with gold particles using gold sputtering to

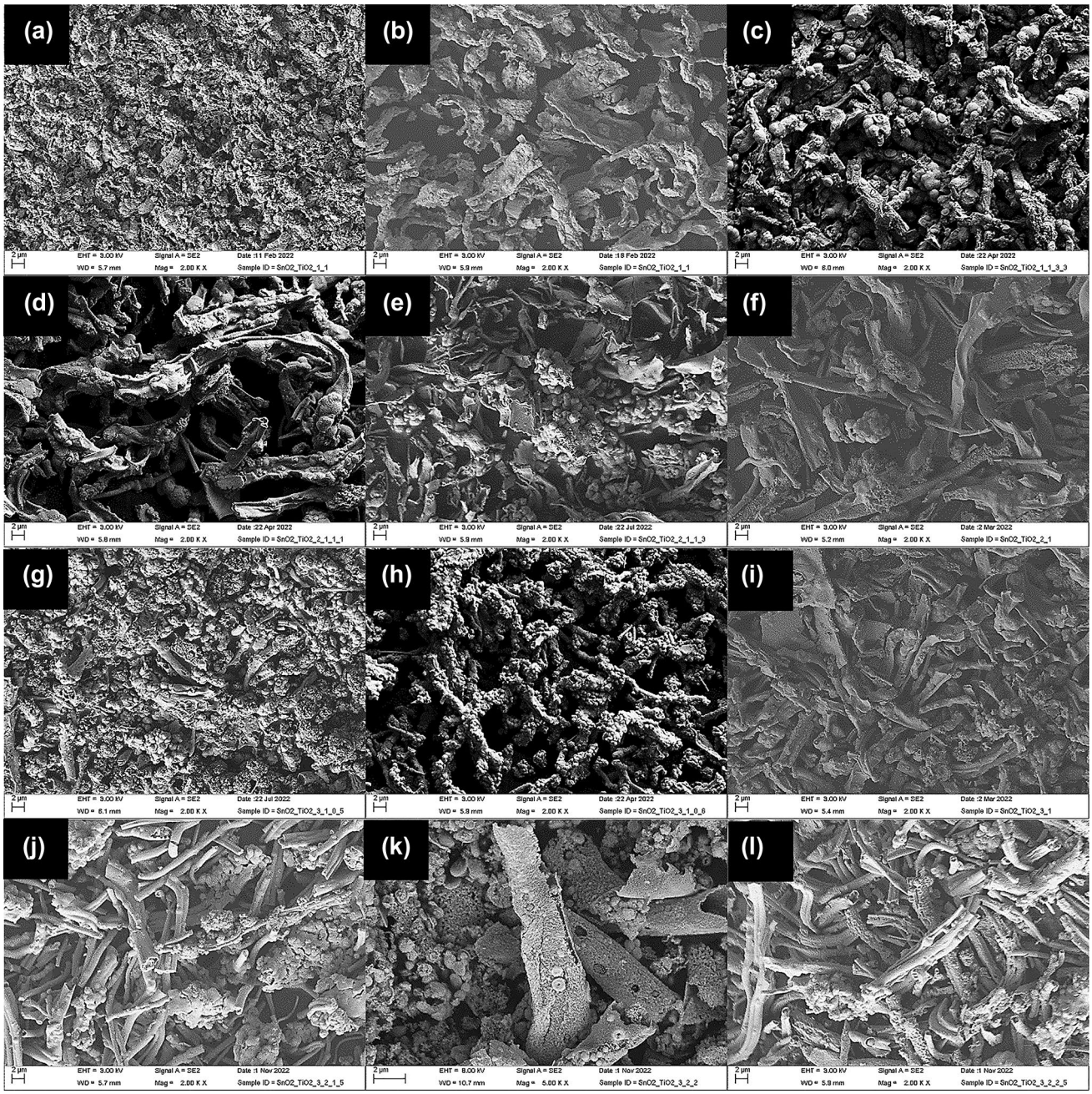

Fig. 3 SEM images of calcined SnO_2/TiO_2 fibers: (1:1) fibers at rates of **a** 1 °C/min, **b** 3 °C/min, and **c** 3.3 °C/min, (2:1) fibers at rates of **d** 1.1 °C/min, **e** 1.3 °C/min, and **f** 1.5 °C/min, (3:1) fibers at rates of **g** 0.5 °C/min, **h** 0.6 °C/min, and **i** 1.0 °C/min, (3:2) fibers at rates of **j** 1.5 °C/min, **k** 2.0 °C/min, and **l** 2.5 °C/min

collect clearer images from SEM and EDS. The diameters of 100 pre-calcined fibers from each ratio were measured and collected to compare, while 100 measurements of length, thickness, and width of calcined short fibers were collected to compare. The fibers were placed in the TGA and heated to 700 °C at a rate of 5 °C/min to examine the thermal degradation of the precursor fibers.

3 Results and Discussion

The morphology and structure of the SnO_2/TiO_2/PVP precursor fibers were analyzed by SEM using an EHT voltage of 3 kV and an SE2 signal at 500 × magnification. Figure 1(a–h) shows the SEM images and the corresponding

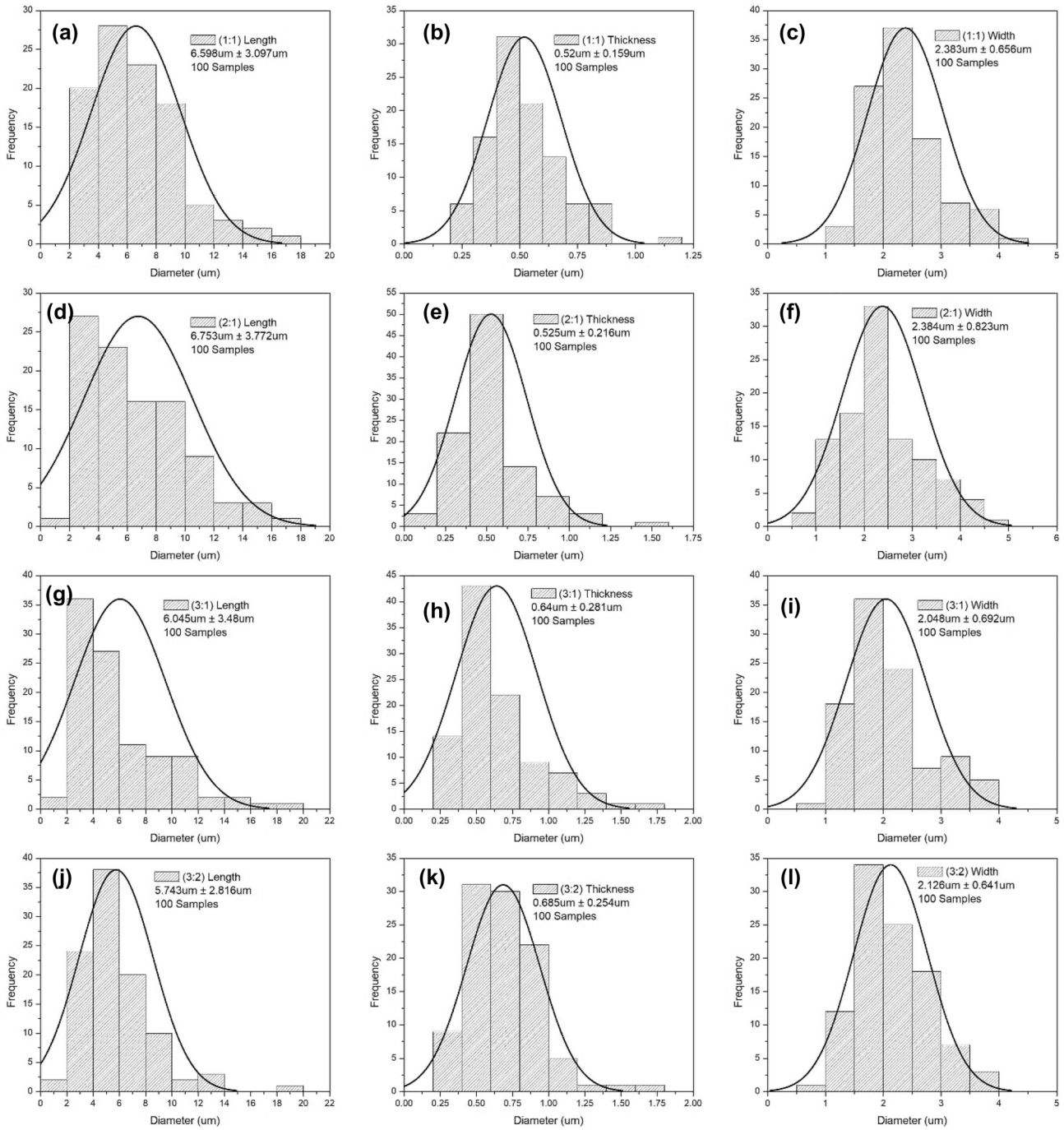

Fig. 4 Length, thickness, and width histograms of SnO_2/TiO_2 calcined fibers: 1:1 (**a**–**c**), 2:1 (**d**–**f**), 3:1 (**g**–**i**), and 3:2 (**j**–**l**)

size distribution histograms of the SnO_2/TiO_2/PVP precursor fibers. The images show long thin fiber morphology with the highest size distribution between 3.5 and 3.8 µm. EDS was used to determine the composition of SnO_2/TiO_2 in the composite fibers using an EHT voltage of 9 kV at 500 × magnification with a resolution of 141.4 eV.

The EDS mappings (Fig. 2) show that the SnO_2/TiO_2/PVP (1:1) composite fibers are composed of distributed carbon (C), nitrogen (N), oxygen (O), tin, and titanium. The EDS mappings of the other ratios are shown in Figs. S1–S3 of the supplementary information (SI). Additionally, Table 1 shows the EDS mapping results of the (1:1) pre-calcined fibers. Based on EDS results, the 1:1 (50%:50%) fibers show a ratio of 45.8%:54.2%. The EDS mapping results of the other ratios are illustrated in (Tables S1–S3) of the supplemental information. The elemental composition results for

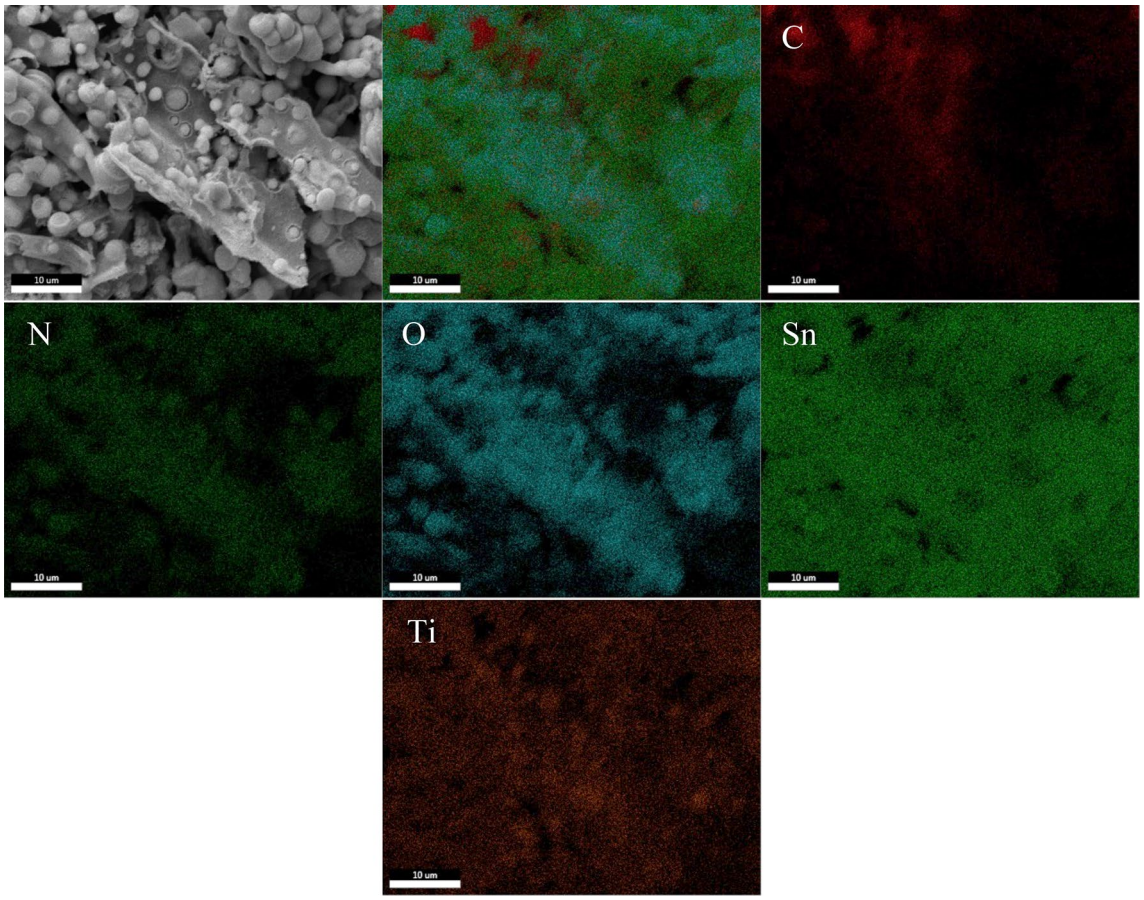

Fig. 5 EDS mapping of SnO_2/TiO_2 (3:2) calcined fibers at 2.0 °C/min

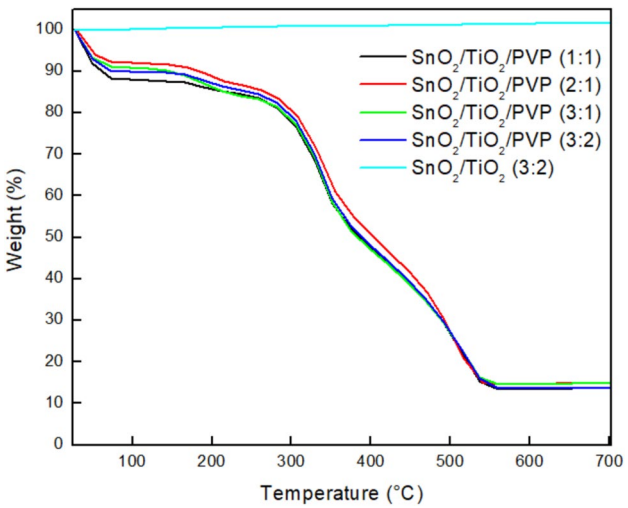

Fig. 6 TGA analysis of SnO_2/TiO_2 pre-calcined and calcined fibers

the other ratios were 62.9%:37.1% for the 2:1 (66%:33%) fibers, 65.3%:34.7% for the 3:1 (75%:25%) fibers, and 54.7%:45.3% for the 3:2 (60%:40%) fibers. These results show that the solutions mixed with the different ratios were spun into pristine fibers with ratios close to the intended mixtures (Table 2).

Figure 3 shows the SEM images of the SnO_2/TiO_2 fibers with 1:1 (a–c); 2:1 (d–e), 3:1 (g–i) and 3:2 (j–l), SnO_2 to TiO_2 ratio, respectively, using an EHT voltage of 3 kV and an SE2 signal at 2000 × magnification. The SnO_2/TiO_2/PVP precursor composite fibers were calcined in a tube furnace using different heating (ramp-up) rates to determine the effect of the heating rate on the micro-belts formation. The rates used for the SnO_2/TiO_2 fibers with (1:1) ratio (Fig. 3 a–c) ranged from 1 to 3.3 °C/min. The SEM image in Fig. 3b shows that the SnO_2/TiO_2 micro-belts were formed after the heat treatment at a rate of 3 °C/min. The SnO_2/TiO_2 prepared at a rate of 1 °C/min (Fig. 3a) showed some micro-belts formation but mostly had random oxidized short fibers. It is worthwhile to note even a low-rate change of 0.3 °C/min (i.e., @ 3.3 °C/min) above the previous rate to form micro-belts, the ramp-up rate caused the fibers to have a completely

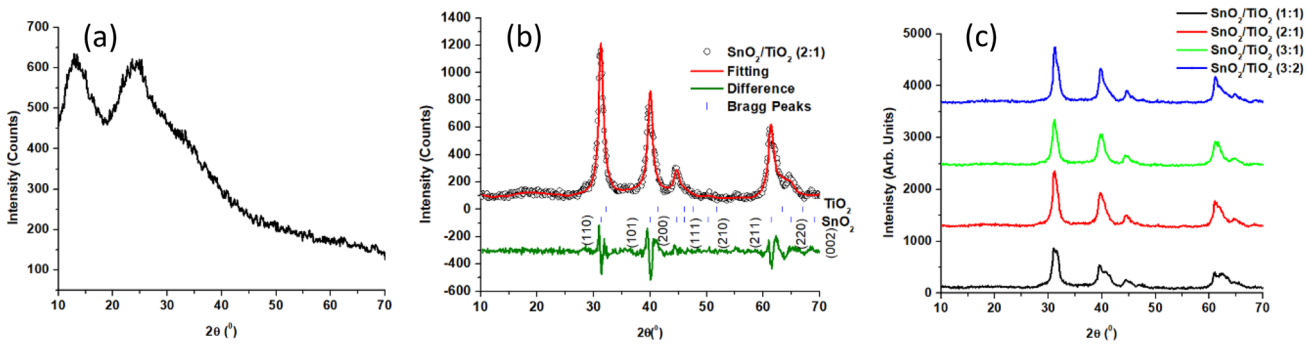

Fig. 7 XRD analysis of **a** SnO_2/TiO_2/PVP fibers, **b** SnO_2/TiO_2 (2:1) calcined fibers, and **c** SnO_2/TiO_2 all ratios

Table 3 LeBail fitting of the SnO_2/TiO_2 (2:1) calcined fibers

Phase	Space Group	*a*(Å)	*b*(Å)	*c*(Å)	*α*(°)	*β*(°)	*γ*(°)	χ^2
TiO_2	$P4_2/mnm$	4.638 (9)	4.638 (9)	3.054 (9)	90.0	90.0	90.0	1.67
SnO_2	$P4_2/mnm$	4.737 (4)	4.737 (4)	3.175 (9)	90.0	90.0	90.0	
TiO_2 [22]	$P4_2/mnm$	4.616	4.616	2.977	90.0	90.0	90.0	N/A
SnO_2 [22]	$P4_2/mnm$	4.737	4.737	3.185	90.0	90.0	90.0	N/A

different morphology (Fig. 3f). The thermal treatment of the precursor fibers using a ramp-up rate of 3.3 °C/min (Fig. 3c) resulted in the formation of short fibers with an abundance of nodules with no definitive shape.

The SEM images of SnO_2/TiO_2 fibers with 2:1 ratio (Fig. 3d–f), prepared at a ramp rate of 1.1 °C/min (Fig. 3d) showed the formation of flat fibers with many nodules. The fibers became wider and flatter at a rate of 1.3 °C/min (Fig. 3e) with fewer nodules than that at 1.1 °C/min. At 1.5 °C/min (Fig. 3f), the SEM images showed the formation of micro-belts.

The SEM images of SnO_2/TiO_2 fibers with 3:1 ratio (Fig. 3 (g-i)), prepared at a ramp rate of 0.5 °C/min (Fig. 3g) showed short fibers with nodules with no definitive shape. The fibers showed no visual difference at a higher rate of 0.6 °C/min (Fig. 3h) than that at 1.1 °C/min. At 1 °C/min (Fig. 3i), the SEM images showed the formation of micro-belts with the indications of the short fibers becoming smooth.

The SEM images of SnO_2/TiO_2 fibers with 3:2 ratio (Fig. 3j–l) showed micro-belts at a rate of 2 °C/min (Fig. 3k). Figure 3j shows that flat belts started to form at a rate of 1.5 °C/min, while the 2.5 °C/min rate (Fig. 3k) showed a few micro-belts started to blend to form bigger nodules.

The SEM images in Fig. 3 showed a pattern for micro-belts formations: the higher the ratio of SnO_2 in the fibers, the slower the ramp-up rate used during the thermal treatment of the SnO_2/TiO_2 precursor fibers. The minimum (or lowest) SnO_2 concentration in the precursor fibers was 50 wt.% for the 1:1 ratio, while the required heating rate for the micro-belts formation was 3 °C/min. The maximum (or highest) SnO_2 concentration in the precursor fibers was 75 wt.% for the 3:1 ratio, while the required heating rate for the micro-belts formation was 1 °C/min. At SnO_2 concentrations of 60 (3:2) and 66 (2:1) wt.%, the heating rates required to form micro-belts were 2 °C/min and 1.5 °C/min, respectively. Alternatively, the pattern can also be described in terms of the TiO_2 concentration in the precursor fibers: the higher the concentration of TiO_2 (25%, 33%, 40%, and 50%), the faster the ramp-up rate needs to be (1 °C/min, 1.5 °C/min, 2 °C/min and 3 °C/min).

Figure 4a–l shows the histograms of length, thickness, and width of the calcined fibers for all the different ratios. The lengths (4a, 4d, 4 g, 4j) for the different ratios have a range between 5.743 and 6.753 µm with the 3:2 ratio being the shortest and the 2:1 ratio being the longest. The fiber thickness (4b, 4e, 4 h, 4 k) is in the range between 0.52 and 0.685 µm with the 1:1 ratio being the thinnest and the 3:2 being the thickest. The widths (4c, 4f, 4i, 4 l) have a range between 2.048 and 2.384 µm with the 3:1 and 2:1 ratio being the thinnest and widest micro-belts, respectively. The results show no pattern of one ratio being the longest, thickest, or widest based on the different ratios. The fibers with different SnO_2:TiO_2 ratios can have different sizes depending on the location chosen for measurements, but the measurements are close to each other that there are no significant differences observed.

Figure 5 shows the EDS mapping of the SnO_2/TiO_2 (3:2) micro-belts. After heat treating at a rate of 2 °C/min, the precursor fibers have carbon, nitrogen, oxygen, tin, and titanium. The EDS mappings of the other calcined

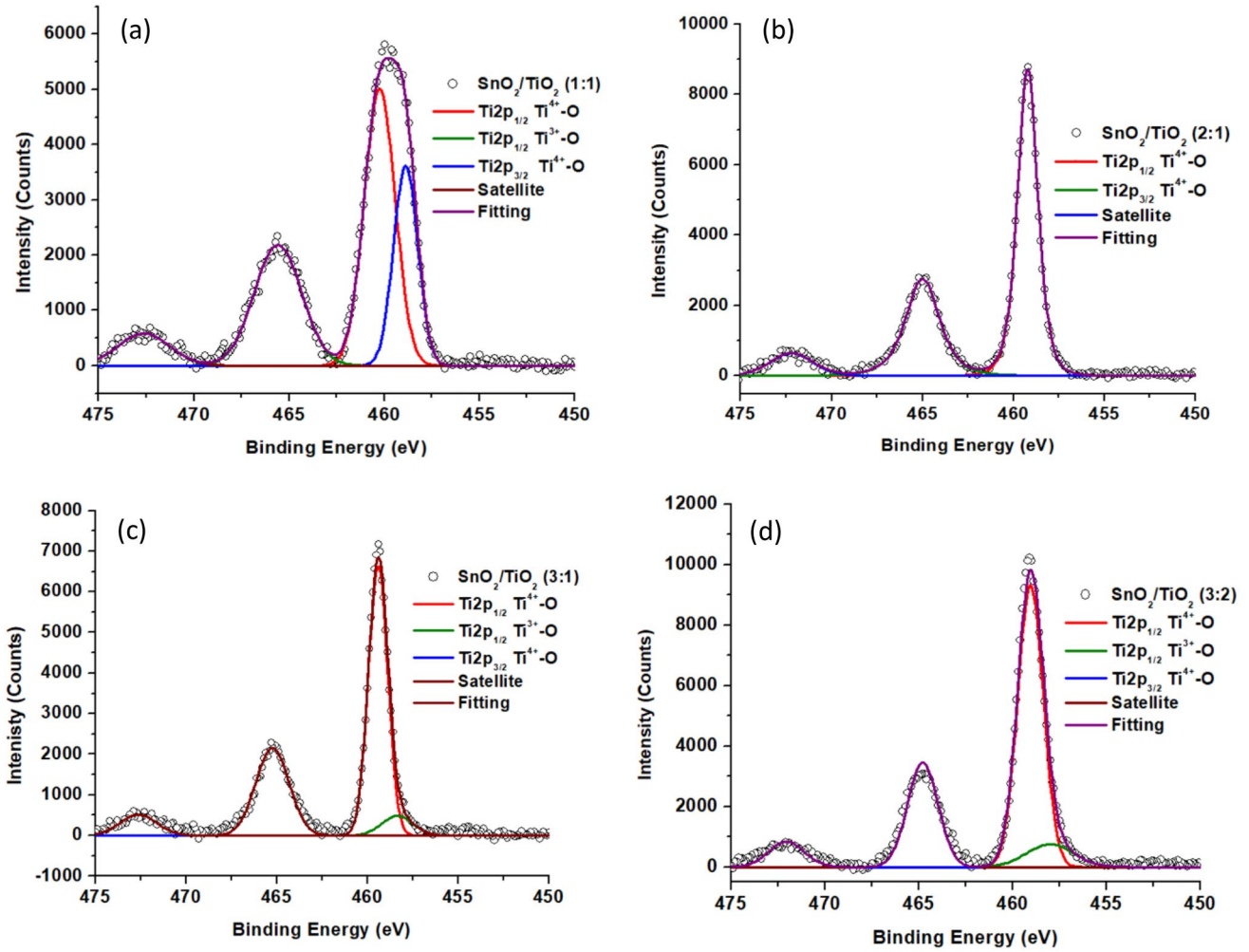

Fig. 8 XPS analysis of $Ti2p_{3/2}$ and $Ti2p_{1/2}$ in SnO_2/TiO_2 **a** 1:1, **b** 2:1, **c** 3:1, and **d** 3:2 calcined fibers

ratios are shown in Figures S1-S3 of the supplementary information (SI).

Figure 6 shows the thermal degradation of the SnO_2/TiO_2/PVP precursor fibers and calcined SnO_2/TiO_2 composite fibers with 3:2 ratio using TGA in air from 27 to 700 °C at 5 °C/min. The results showed that the temperature at which the fibers are stripped of their polymer and solvent, leaving only the active material.

The degradation mechanism of the precursor fibers with different SnO_2 to TiO_2 ratios showed a similar trend. At temperatures between 21 and 100 °C, the weight percentage decreases with increasing temperature which was due to the evaporation of the remaining solvent. Ethanol at this temperature completely evaporates, leaving about 80% of the PVP fibers with the active material. At a temperature between 250 and 525 °C, the weight percentage of the precursor fibers drastically drops from 80 to 15% due to the decomposition of the polymer. At temperatures above 525 °C, the TGA results showed that the content of SnO_2 and TiO_2 in the calcined fibers were 13.6, 14.8, 14.7, and 13.7% for the 1:1, 2:1, 3:1, and 3:2 ratios, respectively. The TGA results for the calcined SnO_2/TiO_2 fibers showed no weight loss upon heating between 550 and 700 °C.

Figure 7a shows the diffraction pattern of the SnO_2/TiO_2/PVP fibers, which only shows weak broad diffraction peaks for the PVP fibers located at 13.1 and 24.0 in 2θ, which are consistent with the position of the diffraction peaks for PVP [26]. Figure 7b shows the fitting of the diffraction pattern for SnO_2/TiO_2 (2:1) composite fibers after calcination, while the fitting results are shown in Table 3, which indicated the presence of both TiO_2 and SnO_2 in the crystal structure of the fibers. The fitting was determined to agree with the results reported on the diffraction patterns of both bulk TiO_2 and SnO_2. From the Le Bail fitting, the χ^2 was determined to be 1.67 (a χ^2 below 5 is considered a good fitting). In the SnO_2 phase, the following Bragg peaks were observed at 110 (31.00°), 101 (39.67°), 200 (44.40°), 111 (45.71°), 210 (49.98°), 211 (61.04°), 220 (64.61°), and 002

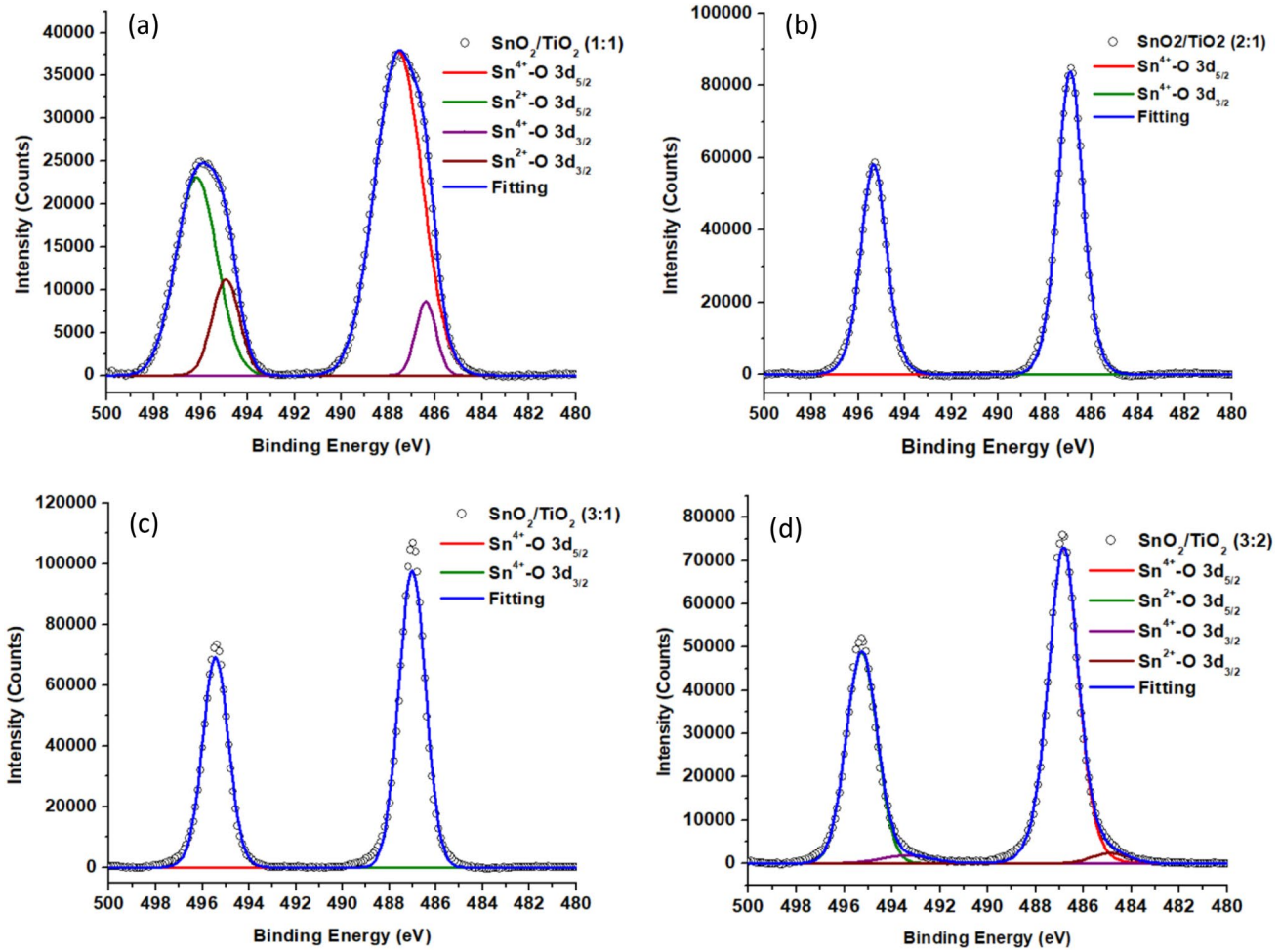

Fig. 9 XPS analysis of $Sn3d_{5/2}$ and $Sn3d_{3/2}$ in SnO_2/TiO_2 **a** 1:1, **b** 2:1, **c** 3:1, and **d** 3:2 calcined fibers

(68.62°), which indicated the presence of a rutile phase of SnO_2 in the sample. The TiO_2 phase showed the following diffraction peaks: 110 (31.91°), 101 (40.99°), 200 (45.76°), 111 (47.22°), 210 (51.53°), 211 (63.10°), and 220 (66.71°), which indicated the presence of a rutile phase of TiO_2 in the sample. Figure 7c shows the diffraction patterns collected for the SnO_2/TiO_2 composite fibers at all the synthesis ratios. The XRD results for Fig. 6c showed that the synthesized samples have consistent diffraction patterns independent of the ratio of Sn:Ti in the precursor fibers, indicating both SnO_2 and TiO_2 in the sample, were present as their respective rutile phases [27–30].

Figure 8a–d shows the XPS spectra collected for the Ti2p which includes the $Ti2p_{3/2}$ and $Ti2p_{1/2}$ regions. The XPS was used with a spot size of 400 um, a pass energy of 25 eV, and an energy step size of 0.1 eV. Figure 8a shows the $Ti2p_{3/2}$ for the SnO_2/TiO_2 at a ratio of 1:1, 8b shows the 2:1 ratio, 8c shows the 3:1, and 8d shows the 3:2 data. All the SnO_2/TiO_2 XPS data for the $Ti2p_{3/2}$ region were deconvolved into two peaks centered at 457.1 and 457.9 which correspond to the presence of some Ti^{3+} and Ti^{4+} bound to oxygen as is observed in TiO_2 [31]. The lower energy TiO_2 may be due to defects present at the surface. For all the samples, the $Ti2p_{1/2}$ peak was determined to consist of one peak centered at 465 eV, which is consistent with Ti^{4+} bound to oxygen as is found in TiO_2. The third peak located around 472 eV corresponds to the Ti2p satellite peak [32]. The XPS data agree with the XRD results in that the titanium oxide present in the sample is present as TiO_2.

Figure 9a–d shows the $Sn3d_{5/2}$ and $Sn3d_{3/2}$ XPS region for the SnO_2/TiO_2 data collected for the samples synthesized at different ratios: 9a shows the 1:1, 9b shows the 2:1 ratio, 9c shows the 3:1 and 9d shows the 3:2 data. Superficially, XPS spectra for all samples are similar with two $Sn3d_{5/2}$ and $Sn3d_{3/2}$ peaks located at 486.8 and 495.3 eV, respectively. The peaks observed at 486.8 eV and 495.3 eV correspond to Sn^{4+}-O binding environment. The XPS results for the SnO_2/TiO_2 composite fibers with 1:1 and 3:2 ratios show an additional peak in the $Sn3d_{5/2}$ and $Sn3d_{3/2}$ regions located at 484.7 and 493.1 eV. The additional peaks may be indicating

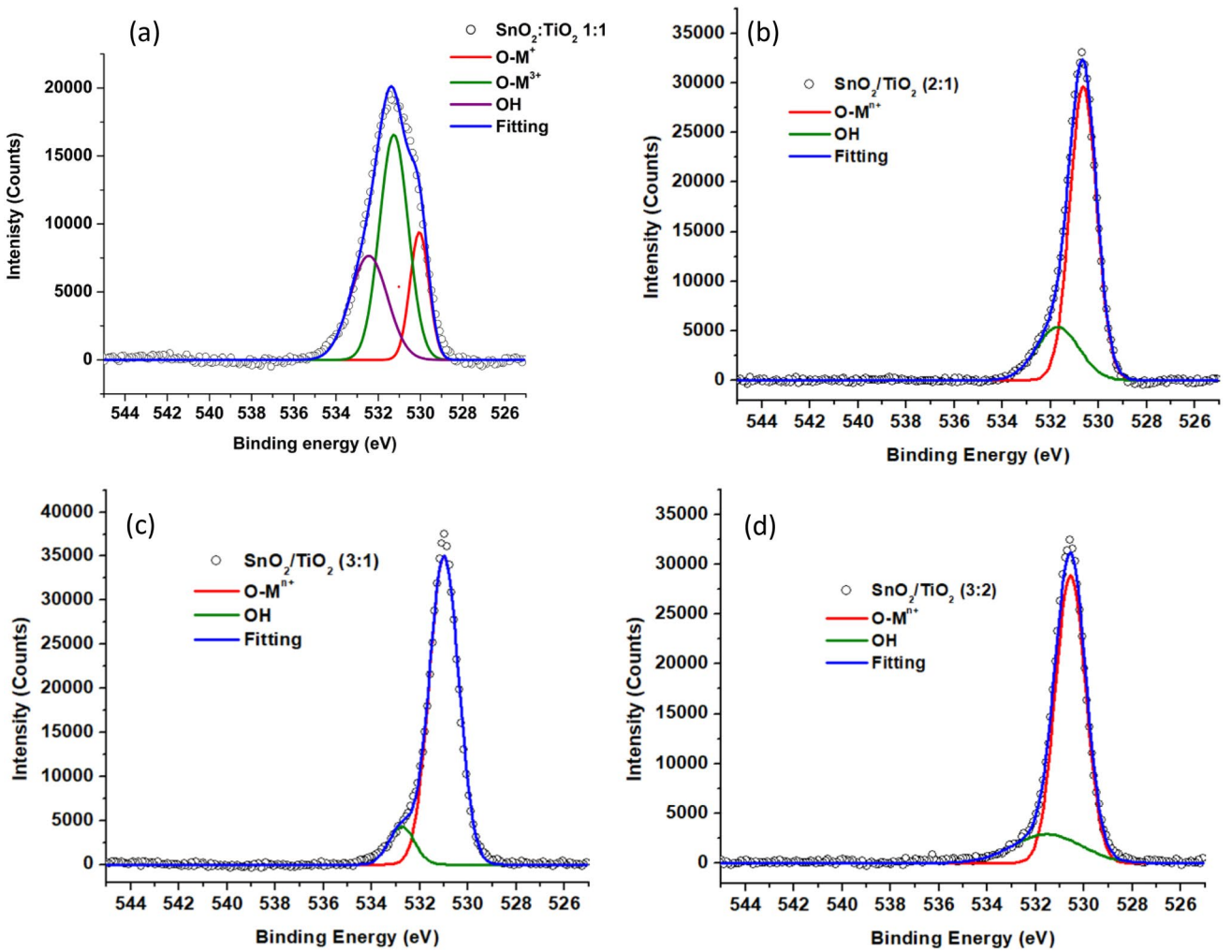

Fig. 10 XPS analysis of O1s spectra in SnO_2/TiO_2 **a** 1:1, **b** 2:1, **c** 3:1, and **d** 3:2 calcined fibers

the presence of a small amount of SnO (Sn(II)O) in the sample as observed in the literature [33].

Figure 10a–d shows the O1s spectra for SnO_2/TiO_2 composite fibers with different ratios: 10a, 10b, 10c and 10d show the spectra for the 1:1, 2:1 3:1, and 3:2 ratios, respectively. The O1s spectra for all samples were deconvolved into two peaks located at 530.7 and 531.6 eV, which have been shown to correspond to oxygen bound to a high oxidation state metal ion such as Ti^{4+} or Sn^{4+} and the presence of oxygen in surface hydroxyl species, respectively[32, 34]. However, the SnO_2/TiO_2 at a ratio of 1:1 shows a higher amount of O than the other samples, this may be due to the formation of carbonate on the surface during the heat treatment [34].

Figure 11a–d shows the C1s XPS spectrum for the SnO_2/TiO_2 calcined fibers with different ratios: 11a, 11b, 11c, and 11d show the spectra for the 1:1, 2:1, 3:1 and 3:2 ratios, respectively. The amount of carbon present in the samples is very low as indicated by the low counts observed in the spectrum. The carbon spectra for all the samples were deconvolved into two peaks located at 285.6 and 288.6 eV, which correspond to C in an Sp3 bond (C–C) and the presence of oxidized carbon (C = O) [34].

Figure 12 shows the Raman spectra for the (a) precursor fibers and (b) SnO_2/TiO_2 composite fibers with 1:1 ratio. Figure 12a shows the spectra vibrations of the precursor fibers at 549, 748, 927, and 1477 cm^{-1}, which are consistent with the Raman spectra found in the literature for PVP fibers [35, 36]. Figure 12b shows the Raman spectra for the SnO_2/TiO_2 (1:1) sample which show the following vibrations, 153.3, 243.1, 341.5, 424.0, 606.36, and 786.8 cm^{-1}. The peaks correspond to a mixture of TiO_2 (rutile phase) and SnO_2 (cassiterite phase) which was observed in the X-ray diffraction patterns. The stretches located 150, 243.1, 445.610, and 610 cm^{-1} correspond to the TiO_2 Rutile B_{1g}, multi-photon processes, E_g, and A_{1g} processes occurring in the TiO_2 rutile materials [37]. In addition, the vibration at 341.5 cm^{-1} can be attributed to multi-photon processes. The SnO_2 Raman vibration for the most part is not visible in the

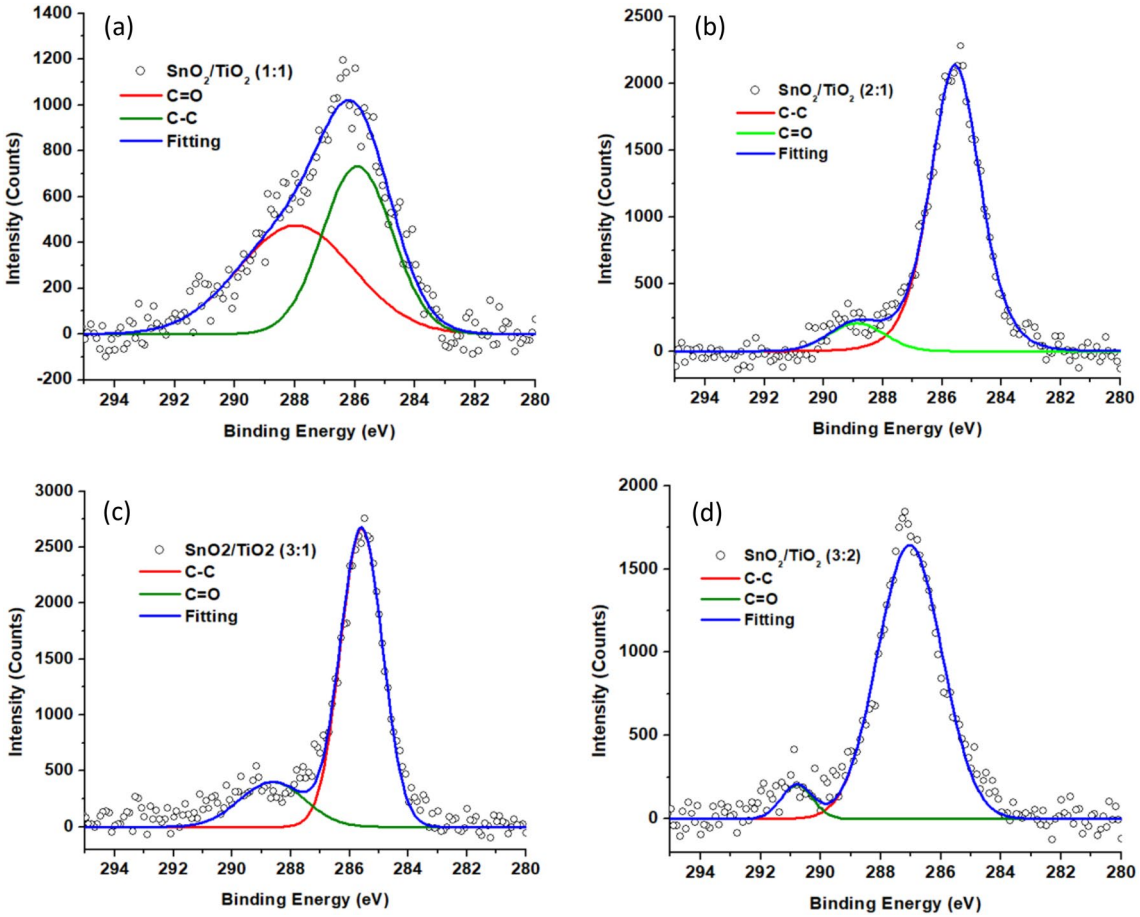

Fig. 11 XPS analysis of C1s spectra in SnO_2/TiO_2 **a** 1:1, **b** 2:1, **c** 3:1, and **d** 3:2 calcined fibers

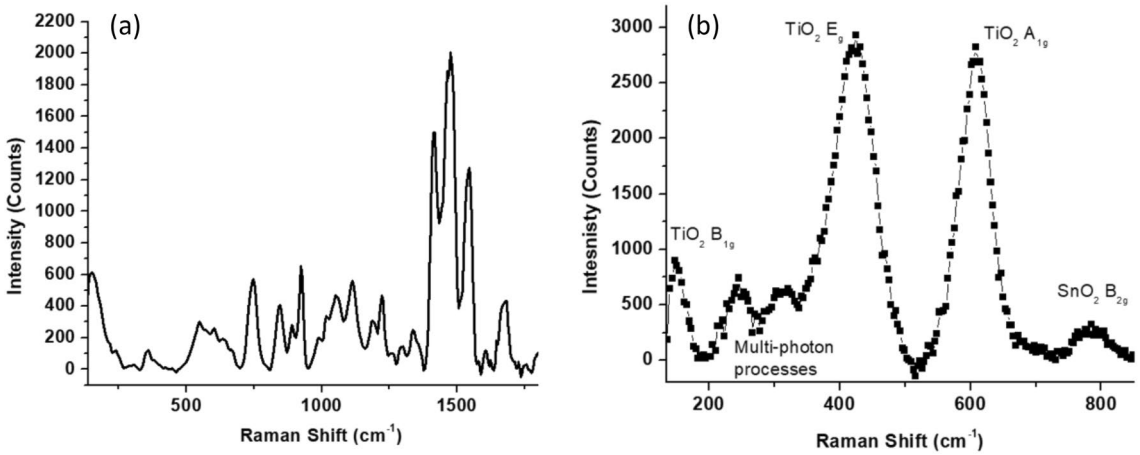

Fig. 12 Raman analysis of **a** SnO_2/TiO_2/PVP pre-calcined fibers and **b** SnO_2/TiO_2 (1:1) calcined fibers

spectrum due to their intensities buried by the TiO_2 rutile vibrations [38]. However, the peak observed at 786.8 cm^{-1} can be characterized as the SnO_2 B_{2g} vibration.

For application purposes, the as-synthesized SnO_2/TiO_2 composite fibers were used as anode materials in Li-ion half cells and their electrochemical performance was evaluated. Figure 13 shows the galvanostatic charge/discharge profiles

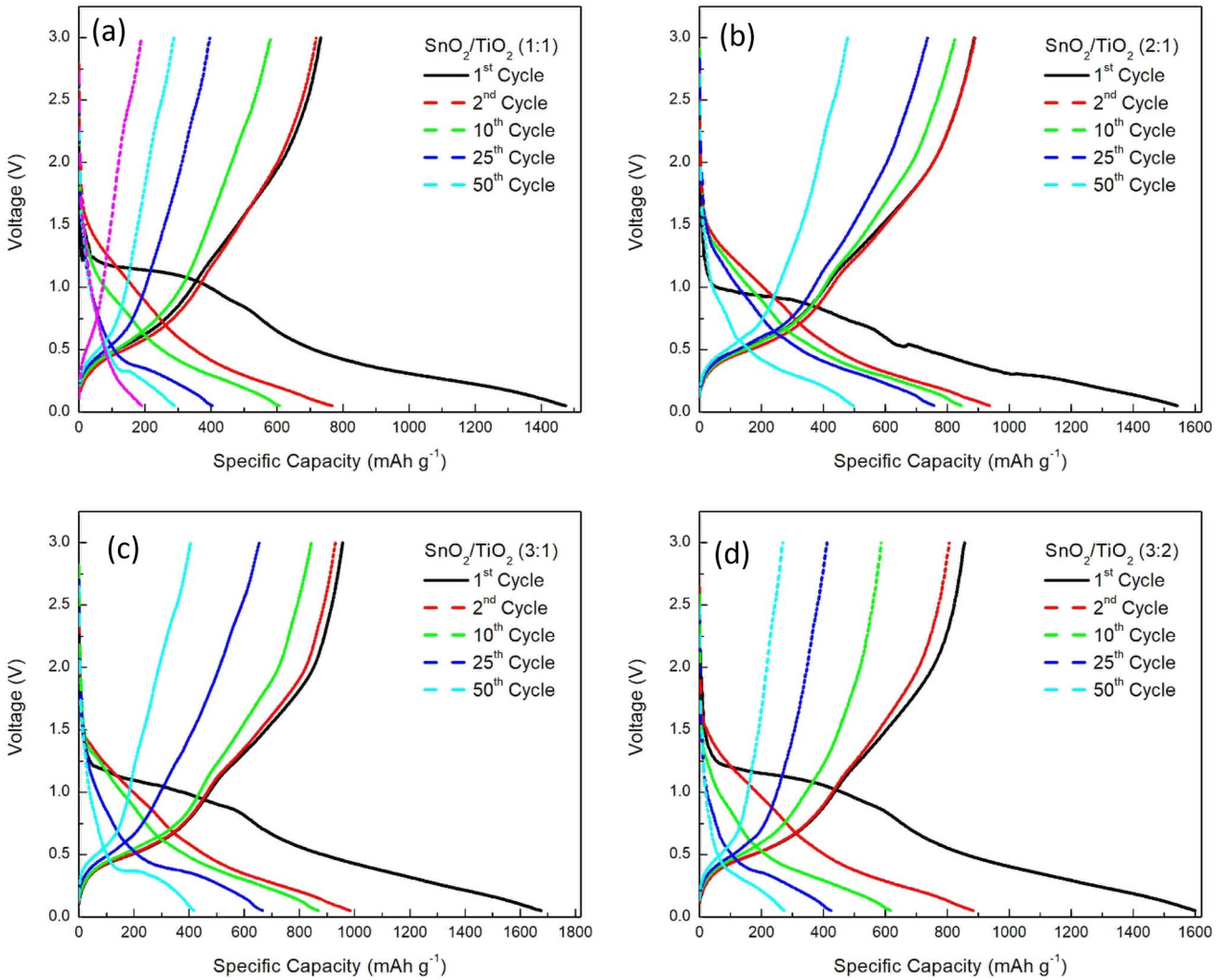

Fig. 13 Galvanostatic charge/discharge profiles of the SnO_2/TiO_2 composite-fiber electrodes with different SnO_2:TiO_2 ratios: **a** 1:1; **b** 2:1; **c** 3:1; **d** 3:2

of the SnO_2 to TiO_2 short-fiber electrodes with different ratios. The charge/discharge experiments were performed for 50 cycles at a current density of 100 mAg^{-1}. The results in Fig. 13 show that there is a large irreversible capacity observed for all SnO_2/TiO_2 composite anodes at the first cycle which mainly is ascribed to the formation of the SIE layer. The results also show a capacity loss at increasing cycle number which is due to the high-volume change of the SnO_2 based electrodes. Figure 14 shows the specific capacity at 50 cycles of the parent metal composites SnO_2 and TiO_2 along with the SnO_2/TiO_2 composite-fiber anodes with different SnO_2 to TiO_2 ratios. The results showed that the SnO_2 and TiO_2 anodes had initial specific capacities of 1337 mAh g^{-1} and 277 mAh g^{-1}, respectively. The SnO_2/TiO_2 composite-fiber anode with 3:1 ratio had the highest initial specific capacity of 956 mAh g^{-1} followed by the 2:1 ratio (886 mAh g^{-1}), the 3:2 ratio (854 mAh g^{-1}), and the 1:1 ratio with the lowest initial specific capacity of 732 mAh g^{-1}. The results showed a pattern of having a higher specific capacity if there was a higher concentration of SnO_2 and a lower specific capacity if there was a higher concentration of TiO_2. After the first charge/discharge cycle, the SnO_2 and SnO_2/TiO_2 composite-fiber anodes showed a capacity fading which was due to the high-volume change during the alloying/dealloying process. After 14 cycles, the SnO_2 sample degraded past the SnO_2/TiO_2 2:1 and 3:1 ratios (~ 800 mAh g^{-1}). After 31 cycles, the SnO_2 sample degraded past the SnO_2/TiO_2 1:1 and 3:2 ratios (~ 350 mAh g^{-1}) and at 35 cycles, the SnO_2 sample degraded past the TiO_2 sample (~ 265 mAh g^{-1}). The results also showed that the SnO_2/TiO_2 composite anode with 3:1 ratio had faster capacity fading when compared to the 2:1 ratio, while the 3:2 ratio had a faster decay in capacity than the 1:1 ratio. This indicated that having a higher content of SnO_2 in the composite electrode

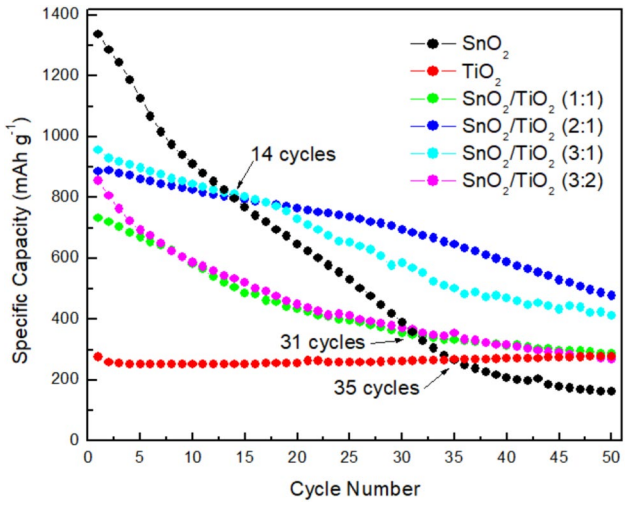

Fig. 14 Charge specific capacity at 100 mA g^{-1} vs. cycle number of the SnO_2/TiO_2 composite-fiber electrodes

resulted in a faster capacity degradation. After 50 cycles, the SnO_2/TiO_2 with 2:1 ratio had the highest specific capacity of 477 mAh g^{-1} at 100 mAg^{-1} followed by the 3:1 ratio (412 mAh g^{-1}), the 1:1 ratio (287 mAh g^{-1}), the TiO_2 sample (278 mAh g^{-1}), the 3:2 ratio (268 mAh g^{-1}), and the SnO_2 sample with the lowest specific capacity of 161 mAh g^{-1}. In fact, the combination of SnO_2 and TiO_2 helped the anode to have a higher specific capacity than TiO_2 (330 mAh g^{-1} [39]) and improved anode degradation compared to SnO_2.

4 Conclusion

In this work, SnO_2/TiO_2 short fibers with different SnO_2 to TiO_2 ratios were successfully prepared by the centrifugal spinning of SnO_2/TiO_2 precursor solutions and subsequent heat treatment at different ramp-up rates. The PVP/ethanol solutions were prepared with using titanium (IV) butoxide and tin (II) 2-ethylhexanoate to generate SnO_2/TiO_2 ratios of 1:1, 2:1, 3:1, and 3:2. The characterization results showed that the morphology of short fibers depended on the ramp-up rates. The results also showed a pattern of having a faster ramp-up rate to obtain micro-belts if the ratio of Sn in the material was high. The EDS mapping showed that the fibers had a chemical makeup of carbon, nitrogen, oxygen, tin, and titanium with numbers close to the intended ratios. The TGA analysis revealed the thermal degradation of the solvent in the fibers as well as the polymer. XRD, XPS, and Raman data showed that both the SnO_2 and TiO_2 were in their respective rutile phases. Furthermore, preliminary electrochemical results showed that the SnO_2/TiO_2 fibers delivered good initial specific capacity due to the SnO_2 and slowed the pulverization of the anode due to the TiO_2. More work is needed to investigate the effect of fiber morphology and structure of the SnO_2/TiO_2 fibers on the electrochemical performance of the composite electrodes.

Supplementary Information The online version contains supplementary material available at https://doi.org/10.1007/s12221-023-00249-x.

Acknowledgements The authors acknowledge the support from the NSF PREM program under Award DMR- 2122178: UTRGV-UMN Partnership for Fostering Innovation by Bridging Excellence in Research and Student Success. This work was partially supported by the Lloyd M. Bentsen, Jr. Endowed Chair in Engineering endowment at UTRGV. The Department of Chemistry at the University of Texas Rio Grande Valley is grateful for the support provided by a Departmental Grant from the Robert A. Welch Foundation (Grant No. BX-0048).

Data availability The data is available from the corresponding author upon request.

Declarations

Conflict of interest The authors declare that they have no conflict of interest.

References

1. M. Toriello, M. Afsari, H.K. Shon, L.D. Tijing, Membranes-Basel **10**(9), 204 (2020)
2. A. Eatemadi, H. Daraee, N. Zarghami, H.M. Yar, A. Akbarzadeh, Artif. Cell Nanomed. B **44**(1), 111–121 (2016)
3. R. O. Chavez, T. P. Lodge and M. Alcoutlabi, Mater. Sci. Eng B-Adv. **266**, 115024 (2021). https://doi.org/10.1016/j.mseb.2020.115024
4. J. Ayala, D. Ramirez, J.C. Myers, T.P. Lodge, J. Parsons, M. Alcoutlabi, J. Mater. Sci. **56**(28), 16010–16027 (2021)
5. J. Lopez, R. Gonzalez, J. Ayala, J. Cantu, A. Castillo, J. Parsons, J. Myers, T.P. Lodge, M. Alcoutlabi, J. Phys. Chem. Solids **149**, 109795 (2021)
6. V.A. Agubra, L. Zuniga, D. De la Garza, L. Gallegos, M. Pokhrel, M. Alcoutlabi, Solid State Ion. **286**, 72–82 (2016)
7. L. Zuniga, V. Agubra, D. Flores, H. Campos, J. Villareal, M. Alcoutlabi, J. Alloys Compd. **686**, 733–743 (2016)
8. R.T. Weitz, L. Harnau, S. Rauschenbach, M. Burghard, K. Kern, Nano Lett. **8**(4), 1187–1191 (2008)
9. H.S. Chen, C.E. Miller, Mater. Res. Bull. **11**(1), 49–54 (1976)
10. J. Gunn, M.Q. Zhang, Trends Biotechnol. **28**(4), 189–197 (2010)
11. X.Z. Wei, X. Kong, C.T. Sun, J.Y. Chen, Chem. Eng. J **223**, 172–182 (2013)
12. X.H. Wang, Y.H. Sang, D.Z. Wang, S.Z. Ji, H. Liu, J. Alloys Compd. **639**, 571–576 (2015)
13. G. Chen, S. Ji, H. Li, X. Kang, S. Chang, Y. Wang, G. Yu, J. Lu, J. Claverie, Y. Sang, H. Liu, ACS Appl. Mater. Interfaces **7**(44), 24950–24956 (2015)
14. Z. Zhao, J. Tian, Y. Sang, A. Cabot, H. Liu, Adv. Mater. **27**(16), 2557–2582 (2015)
15. W. Zeng, T. Liu, Z. Wang, J. Mater. Chem. **22**(8), 3544 (2012)
16. M.F. Hassan, Z.P. Guo, Z. Chen, H.K. Liu, J. Power Sources **195**(8), 2372–2376 (2010)
17. F.C. Zheng, K. Shi, S.H. Xu, X.Y. Liang, Y.C. Chen, Y.G. Zhang, RSC Adv **6**(12), 9640–9646 (2016)

18. L.Q. Mai, B. Hu, W. Chen, Y.Y. Qi, C.S. Lao, R.S. Yang, Y. Dai, Z.L. Wang, Adv. Mater **19**(21), 3712–3716 (2007)
19. Q. Tian, L. Li, J. Chen, L. Yang, S.-I. Hirano, J. Power Sources **376**, 1–10 (2018)
20. G. Gonzalez, M.T. Hasan, D. Ramirez, J. Parsons, M. Alcoutlabi, Polym. Eng. Sci. **62**(2), 360–372 (2022)
21. W. Zhou, H. Liu, J. Wang, D. Liu, G. Du, J. Cui, ACS Appl. Mater. Interfaces **2**(8), 2385–2392 (2010)
22. Y. Wang, G. Du, H. Liu, D. Liu, S. Qin, N. Wang, C. Hu, X. Tao, J. Jiao, J. Wang, Z.L. Wang, Adv. Funct. Mater. **18**(7), 1131–1137 (2008)
23. F.L. Zheng, G.R. Li, Y.N. Ou, Z.L. Wang, C.Y. Su, Y.X. Tong, Chem. Commun. (Camb) **46**(27), 5021–5023 (2010)
24. C.X. Wang, L.W. Yin, L.Y. Zhang, D. Xiang, R. Gao, Sens.-Basel **10**(3), 2088–2106 (2010)
25. V.D. Nguyen, V.H. Nguyen, T.H. Pham, D.C. Nguyen, M. Thamilselvan, J. Yi, Physica E **41**(2), 258–263 (2008)
26. C.S. Ramya, S. Selvasekarapandian, T. Savitha, G. Hirankumar, P.C. Angelo, Physica B **393**(1–2), 11–17 (2007)
27. R.J. Swope, J.R. Smyth, A.C. Larson, Am. Mineral **80**(5–6), 448–453 (1995)
28. E.P. Meagher, G.A. Lager, Can. Mineral **17**, 77–85 (1979)
29. W.H. Baur, A.A. Khan, Acta Crystall. B-Stru B **27**(Nov15), 2133–3000 (1971)
30. W.H. Baur, Acta Crystallogr. **9**(5), 515–520 (1956)
31. D. Toloman, O. Pana, M. Stefan, A. Popa, C. Leostean, S. Macavei, D. Silipas, L. Perhaita, M.D. Lazar, L. Barbu-Tudoran, J. Colloid Interf. Sci. **542**, 296–307 (2019)
32. T.H. Huy, B.D. Phat, F. Kang, Y.F. Wang, S.H. Liu, C.M. Thi, S.J. You, G.M. Chang, P.V. Viet, Chemosphere **215**, 323–332 (2019)
33. M. Kwoka, L. Ottaviano, M. Passacantando, S. Santucci, G. Czempik, J. Szuber, Thin Solid Films **490**(1), 36–42 (2005)
34. H.M. Shi, M. Zhou, D.F. Song, X.J. Pan, J.C. Fu, J.Y. Zhou, S.Y. Ma, T. Wang, Ceram Int. **40**(7), 10383–10393 (2014)
35. G. Agrawal, S.K. Samal, Acs Biomater. Sci. Eng. **4**(4), 1285–1299 (2018)
36. D.L.A. de Faria, H.A.C. Gil, A.A.A. de Queiroz, J. Mol. Struct. **478**(1–3), 93–98 (1999)
37. O. Secundino-Sanchez, J. Diaz-Reyes, J.F. Sanchez-Ramirez, J.L. Jimenez-Perez, Rev. Mex. Fis. **65**(5), 459–467 (2019)
38. A. Leonardy, W.Z. Hung, D.S. Tsai, C.C. Chou, Y.S. Huang, Cryst. Growth Des. **9**(9), 3958–3963 (2009)
39. Y. Liu and Y. F. Yang, J Nanomater. **2016**, 8123652 (2016). https://doi.org/10.1155/2016/8123652